sustainability

Article

Aerodynamic Force and Aeroelastic Response Characteristics Analyses for the Galloping of Ice-Covered Four-Split Transmission Lines in Oblique Flows

Zhaoqing Chen [1,2], Weijie Cai [1,2], Jin Su [1,3], Bo Nan [4,*], Cong Zeng [1,2] and Ning Su [5]

[1] School of Civil Engineering and Architecture, Northeast Electric Power University, Jilin City 132012, China
[2] Key Lab of Electric Power Infrastructure Safety Assessment and Disaster Prevention of Jilin Province, Northeast Electric Power University, Jilin City 132012, China
[3] Heilongjiang Electric Power Design Institute Co., Ltd., China Energy Engineering Group, Harbin 150078, China
[4] College of Water Conservancy, Shenyang Agricultural University, 120 Dongling Road, Shenyang 110866, China
[5] Tianjin Research Institute for Water Transport Engineering, Ministry of Transport, Tianjin 300456, China
* Correspondence: nanbo@syau.edu.cn

Abstract: In order to study the galloping mechanism of ice-covered four-split transmission lines in oblique flows, the aerodynamic forces and aero-elastic response characteristics of the crescent-shaped four-split ice-covered transmission lines are investigated through wind tunnel tests on rigid and aero-elastic models. According to Den Hartog and Nigel's galloping theories, the damping coefficients are calculated based on the experimental data. The results show that the crescent-shaped ice-covered four-split transmission lines usually suffer from torsional galloping. Furthermore, based on the aero-elastic wind tunnel data, the galloping is characterized by an elliptical trajectory, negative damping ratio, and a negative strain at hanging position. In addition, the galloping appears to be more prone to occur under oblique flows, with a larger galloping amplitude and a lower critical wind speed. This might be because an out-of-plane vibration of the third-order mode is excited at a lower wind speed, leading to a coupled resonance between in-plane and out-of-plane vibrations at the third-order mode with a frequency ratio of 1:1. The experimental results in this paper can also be used to verify the fluid-structure interaction simulation method of ice-covered transmission lines.

Keywords: ice-coated transmission line; galloping; aero-elastic model; wind tunnel test; oblique flows; aerodynamic coefficients

Citation: Chen, Z.; Cai, W.; Su, J.; Nan, B.; Zeng, C.; Su, N. Aerodynamic Force and Aeroelastic Response Characteristics Analyses for the Galloping of Ice-Covered Four-Split Transmission Lines in Oblique Flows. *Sustainability* **2022**, *14*, 16650. https://doi.org/10.3390/su142416650

Received: 25 October 2022
Accepted: 10 December 2022
Published: 12 December 2022

1. Introduction

For a power system build in a cold region, where the transmission lines are iced, the section shapes become non-circular, leading to a change of the aerodynamic force characteristics. At a specific range of wind attack angles and wind speeds, the ice-covered conductor will absorb energy from the wind, leading to a divergent vibration, and so galloping occurs.

Due to a wide application of overhead transmission lines that pass through regions with different climates, icing of transmission lines is a common phenomenon, particularly in extreme weather conditions. Galloping has brought disasters to long-distance power transmission, such as damages of metal clips, breakages of conductors, collapses of towers, etc. With the development of economy, the demand for power transmission is growing as more transmission lines are built. As a result, the loss caused by galloping disasters is also growing. Therefore, the observation, simulation, and mechanism researches of galloping has become of great interest to scholars worldwide.

Some scholars observed the galloping response of realistic transmission lines to study the galloping characteristic and seek measures to reduce galloping. For example, Dyke [1] observed the galloping amplitude on the transmission lines of the D-shaped icing section. It was found that the wind direction angle had a significant effect on the galloping amplitude of transmission lines. Hung et al. [2] discussed the response characteristics based on in-situ measurement. The mean wind speed, wind direction, and power spectral density (PSD) were analyzed to identify the vibration types. Gust response analysis was carried out in the frequency domain after the eigenvalue analysis to reproduce the field observation results. Gurung et al. [3] proposed a method of multiple modal analysis, consisting of the random decrement method (RDM) and Eigensystem realization algorithm (ERA), to identify galloping. Based on the tested results obtained from the Tsuruga Test line, the effectiveness of the method was validated. In summary, a series of measures are mentioned to prevent or reduce the galloping of the transmission lines. However, due to the limitation of the monitoring equipment, these early monitoring studies could only capture limited information of the galloping, which prohibits the understanding of the galloping mechanisms. Recently, some scholars [4–6] tried to design and adopt advanced facilities and techniques, such as target detection of infrared source, unmanned aerial vehicle remote sensing image, and deep neural networks, to monitor the galloping of conductors. Other scholars have tried to design devices [7] to control the vibration of galloping. At present, the on-site monitoring of galloping is still a difficult task. Due to the complexity of galloping, a single galloping prevention device is almost impossible to completely solve the problem.

The theoretic research on the galloping mechanism of iced conductor can be traced back to the 1930s. Den Hartog [8] tested the variation of the aerodynamic force coefficients of the iced non-circular cross-section conductor with respect to the wind attack angle. A simplified single-degree-of-freedom iced conductor model was established to predict vertical galloping. It is considered that the vertical galloping occurs when the negative derivative of the aerodynamic lift curve is greater than the damping effect caused by the aerodynamic drag. Through theoretical and experimental research, Nigel [9] found that when the aerodynamic torsional damping is negative and its absolute value is greater than the torsional damping of the conductor, torsional self-excited vibration instability occurs, which is also known as the Nigel galloping mechanism. Yu et al. [10,11] proposed a mechanism of inertial coupling galloping based on the study of galloping characteristics of an eccentric iced conductor. These theories are widely adopted as fundamental landmarks for the galloping mechanism of iced conductors. However, it is still difficult to explain all the galloping phenomena in practical engineering.

Some scholars measured the aerodynamic force of iced conductors with different shapes and splitting numbers through wind tunnel tests. The influences of wind speed, wind attack angle, and other parameters on galloping characteristics were investigated. For example, Guo et al. [12,13] proposed an experimental method to study the galloping characteristics of an ice-coated four-split conductor. Lou et al. [14–16] tested the aerodynamic coefficients of eight-split conductors and proposed a galloping stability criterion for the 3-DOF coupled motion of an ice-accreted conductor. Xie et al. [17] tested the global drag coefficients of multi-split transmission lines with different diameters and split numbers, which were subjected to different turbulence intensities and wind attack angles. Others, such as Huang [18], Chabart and Lilin [19], Zdero [20], Li et al. [21], and Zhou et al. [22], conducted wind tunnel tests with iced single or multi-split (four-, six-, or eight-split) transmission line models supported by springs. All the studies mentioned above provide references for engineering practices. It is summarized that the galloping of the transmission line is greatly affected by the wind speeds, the ice-covered shapes, and the approaching flow directions.

Some scholars tried to study the galloping mechanism of transmission lines from the resonance of in-plane and out-of-plane modes. Bartoli et al. [23] studied the characteristics of the vibration modes and the frequencies of single-span cables. It was found that the modal functions of a single transmission line can be divided into symmetric and asymmetric modes, which are independent of each other. Rega et al. [24,25] analyzed the influence of suspension conditions on the resonance generation. The relationship between the cable vibration amplitude and the intrinsic natural frequency was established. Benedettini [26] investigated the simultaneous existence of resonance within the frequency ratio of 1:1 and 1:2 in suspension cable structures. It was verified that in-plane, out-plane, symmetric, and anti-symmetric modes of the cable structure are strongly coupled when the geometric parameters satisfy certain conditions. Liu et al. [27–29] proposed the theoretical formulation of the out-of-plane modes and the corresponding frequencies of the continuous transmission line by establishing the differential equation based on continuity condition. Nino et al. [30] and Ferretti et al. [31] analyzed the nonlinear aero-elastic behavior of cables undergoing dynamical in-plain galloping. Nie et al. [32,33] studied the internal resonance response of an L-shaped beam structure, considering quadratic and cubic nonlinearities. The in-plane and out-of-plane resonance theories can be used in discussing the galloping conditions of iced conductors from the perspective of the whole span, which provides a useful supplement to the vertical and torsional galloping mechanism.

Some other scholars have tried to reproduce the galloping process of iced conductors numerically. Yan [34,35] established a galloping model for ice-covered transmission lines based on the spatial curved beam theory. It was found that the ice-covered thickness has a large effect on the critical wind speed. In addition, the wind direction angle of attack has a significant influence on the galloping type. Wu et al. [36] used FLUENT software to simulate the air flow around iced conductors. Liao et al. [37] and Ding et al. [38] proposed some novel types of energy harvester based on the galloping of a flexible model and simulated the vortex pattern and velocity distributions contours around the model. Antonio et al. [39] simulated the galloping vibration of the D-section model numerically and proposed a kinematic rotary control method to enhance energy harvesting from transverse galloping. Meynen et al. [40] simulated the wind energy input of a single conductor numerically by solving a two-dimensional laminar simple harmonic oscillation cylinder problem. Clunia et al. [41] analyzed the fatigue life of a transmission line under wind loads using numerical simulations in laminar and turbulent flow. The axial force, total resistance, and mid-span displacement at the conductor support were obtained. These numerical simulation studies aims at revealing the interaction process between fluid and structure, and the causes of galloping of iced conductors were discussed, which are beneficial in clarifying the galloping mechanism of iced conductors. However, in practical engineering, due to the complex environment, boundary conditions are difficult to be reproduce when the iced conductor is galloping. Most current numerical simulation studies are carried out for simplified models, which is not applicable in practice, and they cannot fully reproduce the galloping process of all iced conductors.

In summary, most current researches on the galloping mechanism of ice-covered transmission lines are mainly focused on the situation that the incoming flow is perpendicular to the conductor span. However, in the field investigation of galloping disasters, it was found that when there is a certain angle between the incoming flow and the span of transmission line, the galloping wind speed is lower and the galloping amplitude is larger. At present, there are still few studies on this aspect. Therefore, the research on the galloping characteristics of four-split transmission lines in oblique flows are still lacking.

To explore whether the galloping is more prone in oblique flows, and to further investigate the influence of wind direction on the galloping amplitude, a series of aerodynamic force test experiments were carried out, firstly to determine the aerodynamic coefficients of ice-covered four-split conductor, then the galloping type of the structure was determined based on Den Hartog and Nigel's theories. After that, the wind-induced response of an aero-elastic ice-covered four-split transmission line model, which had the same icing parameters with the force test model, was measured under different wind directions and wind speeds. At last, the galloping characteristics of the ice-covered four-split transmission line under different wind directions were analyzed.

For the convenience of reference, all notations used in this paper are described in Abbreviations.

2. Wind Tunnel Test

In this study, two sets of tests, including a six-component force measurement test on the rigid model and a vibration measurement test on the aero-elastic model, were carried out. The aerodynamic forces of the ice-covered four-split conductor under different wind attack angles was measured through the force measurement test to determine the type of galloping. The aero-elastic model test was carried out to measure the wind-induced responses of the ice-covered four-split transmission line model under different wind direction angles, and the influence of oblique flows on the galloping characteristics of transmission lines was studied.

The test was carried out in the atmospheric boundary layer wind tunnel TKS-400 in the Tianjin Research Institute for Water Transport Engineering (TIWTE). The wind tunnel was an open-circuit wind tunnel. The test section of the wind tunnel was 4.4 m in width, 2.5 m in height, and 15 m in length. The initial pressure for the wind tunnel was 8.5 Pa and the average temperature in the wind tunnel was approximately 21.2 °C.

2.1. Test Setups

2.1.1. Six-Component Force Measurement Test

To study the aerodynamic characteristics of the four-split conductor, a group of four-split conductor models with the same shape as the aero-elastic models were manufactured. According to the actual transmission line erection size and ice-covered conditions, the conductor type LGJ-500/35 was assumed as the prototype of a crescent-shaped four-split transmission line. The scale ratios of the iced-coated thickness and splitting distance is 4.5:1. The model schematic diagrams of the cross-section of the ice-covered transmission line and spacer are shown in Figure 1, where Ø represents the diameter of the circle. The cross-section shape of the ice is crescent, the axial split distance of the conductor model is 100 mm.

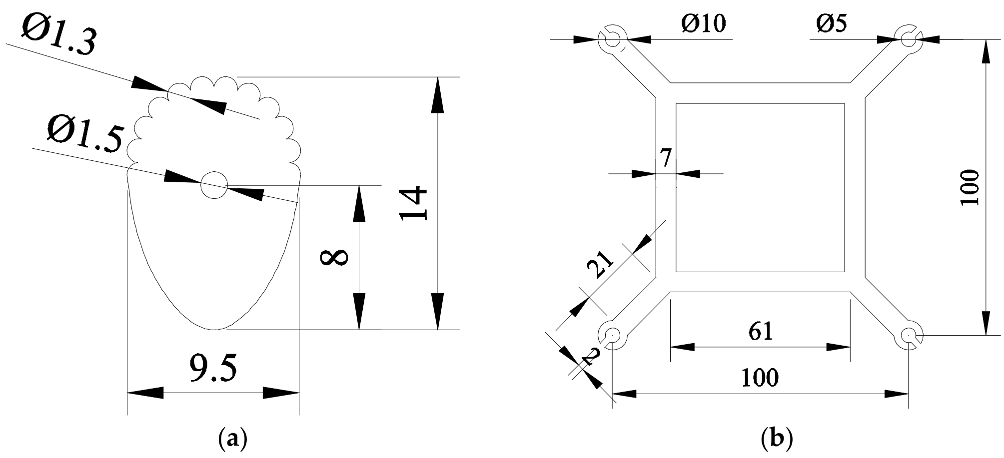

Figure 1. Schematic diagrams of ice cross section and spacer for the model (Unit: mm): (**a**) Ice cross section. (**b**) Spacer.

The photos of the aerodynamic force test of ice-covered four-split conductors are shown in Figure 2. As shown in Figure 2a, in the force measurement test, one of the models of ice-covered four-split conductor was installed on a six-component balance to measure its force and torque along the x, y, and z directions. The length of the ice-covered conductor model is 35 cm. Figure 2b shows the directions for x, y, and z directions. In order to ensure that the airflow at the upper end of the iced conductor model was consistent with that of the real conductor, an end plate was installed at the upper end of the ice-covered four-split conductor model, as shown in Figure 2c. The sampling frequency of the six-component force balance is 1024 Hz. Three groups of data were sampled each time, and the sampling time of each group of data is 30 s.

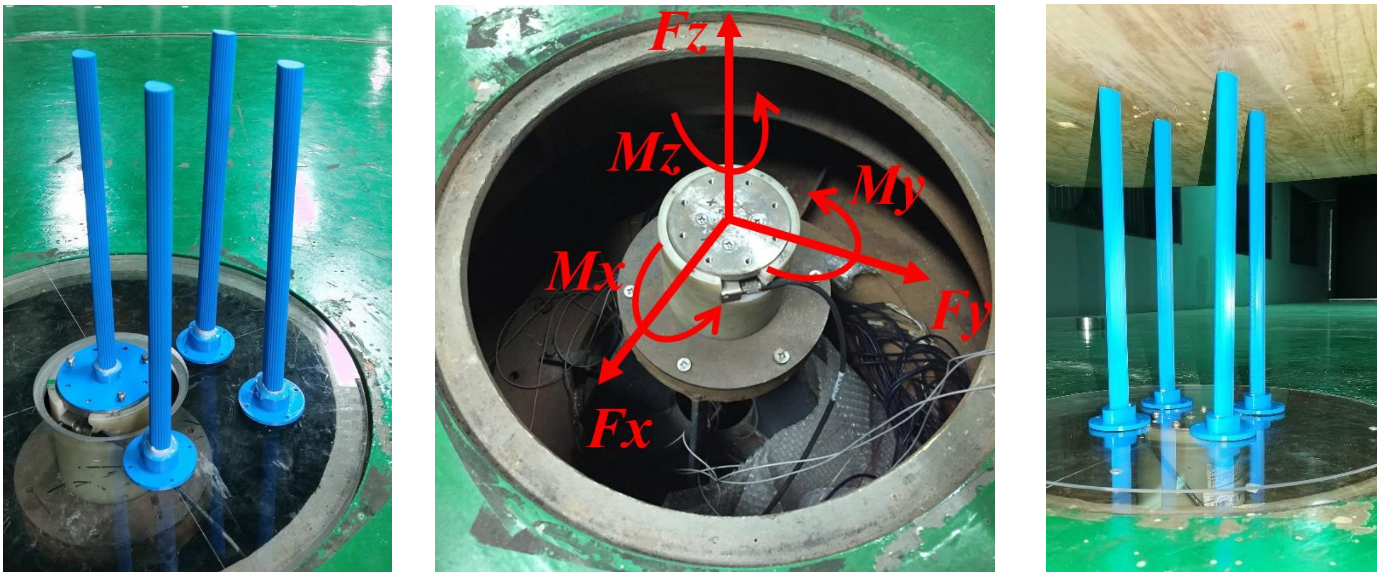

(a) (b) (c)

Figure 2. Photos of aerodynamic force test of ice-covered four-split conductors: (**a**) Connection of ice-covered conductor model and six-component balance. (**b**) Setting up of end plate. (**c**) Force direction of six-component balance.

The definition of incoming flow axis, aerodynamic axis, and wind angle of attack are shown in Figure 3, where F_L and F_D represent the lift and drag forces of the ice-covered conductor model along the incoming flow axis, and F_x and F_y represent the x and y direction forces along the axis of the six-component force balance, respectively. M_x, M_y, and M_z represent the x, y, and z direction moment along the axis of the six-component force balance, respectively. Letter α represents the wind attack angle. The test was carried out in uniform flow with a wind speed of 10 m/s, which referred to the average wind speed of the wind speed measurement point where the Cobra probe was located. The wind attack angle α increased from 0° to 180° with an interval of 10°.

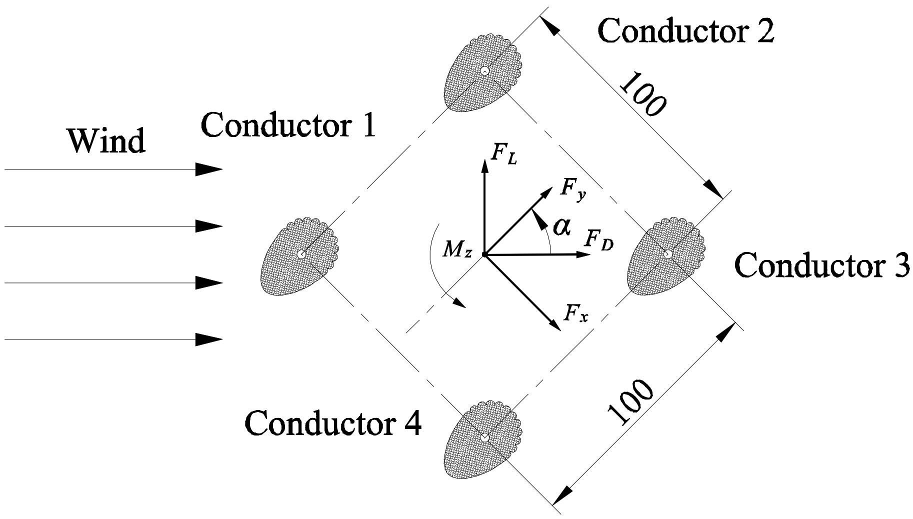

Figure 3. Definition of incoming flow axis, six-component force balance axis and wind angle of attack (Unit: mm).

2.1.2. Vibration Measurement Test on an Aero-Elastic Model

According to the similarity theory, in an aero-elastic model wind tunnel test, the similarities regarding geometric, flow field, and structural vibration parameters should be satisfied. However, due to the complexity, the involved similarity parameters cannot be completely satisfied at the same time. Therefore, it is necessary to select some crucial similarity criteria according to the research problem, and relax the secondary or uncontrollable parameters.

In the design process of the aero-elastic model, the basic scale ratios are first determined, and then other scale ratios are derived. The basic scale ratios include the geometric scale ratio λ_L and the wind speed ratio λ_U. The basic scale ratio can be independently determined according to the experimental conditions. The geometric scale ratio considers the blocking rate to be less than 5%, which is determined as λ_L = 1:40 according to the dimension of the wind tunnel. The wind speed ratio λ_U is set as 1:1. The wind speed of the wind tunnel test is determined as 3~9 m/s. The density ratio is set as 1:1. In addition, the other scale ratios (such as the conductor diameter) are determined according to the wind tunnel test, and the specific parameters of the model are shown in Table 1. The prototype of the transmission line is set with three spacers. To maintain consistency, the aero-elastic model is also designed with three spacers, and install one hanger clip each. In order to keep the four transmission lines in parallel, two spacers are also installed at both ends of the test model.

Table 1. Dimensions of prototype and scale ratios of the aero-elastic model.

Physical Quantity	Prototype	Model	Scale Ratio
Span	160 m	3.5 m	40:1
Transmission line diameter	30 mm	1.5 mm	20:1
Splitting distance	450 mm	100 mm	4.5:1
Mean iced-coated thickness	47.5 mm	9.5 mm	4.5:1
Maximum sag at mid-span	8 m	400 mm	20:1
Wind speed	3–9 m/s	3–9 m/s	1:1

It should be noted that due to the limitation of the width of the wind tunnel laboratory, the scale ratio of the icing section and the span of the transmission line was not the same. Therefore, it is difficult to accurately calculate the response results measured by the test to the field ice-covered transmission line. the purpose of the experiment is to explore whether there is a possibility that the occurrence of galloping in oblique wind direction is easier, and the amplitude is larger than that when the incoming flow is perpendicular to the transmission line span direction. Therefore, the error caused by the scale ratio dissatisfaction is believed to also be acceptable.

Figure 4 shows the installation schematic diagram of the aero-elastic model. The test model consists of two equivalent towers and a crescent ice-covered four-split transmission line model. Four parallel iced conductors are connected to each other through five spacer models at the five different positions of 0, L, $L/4$, $L/2$, 3 $L/4$, and L to form an ice-covered four-split transmission line model. L represents the span of the transmission line. The stiffness of the conductor is simulated by a wire rope with a diameter of 1.5 mm with an elastic modulus of 1.86 GPa, and the wire rope is covered with a semi-circular elliptic shape polylactic acid (PLA) material icing model at a 10 cm spacing. The equivalent tower is composed of a vertical bar, horizontal bar, anchor support, and insulator model. There are four positions of T_1, T_2, T_3, and T_4 for the equivalent towers to set up. One end of the four-split iced transmission line model is suspended under the insulator model (modeled by a spring) of the equivalent tower at the T_4 position through the spacer model, another end of the model is adjustable by adjusting the equivalent tower T_1, T_2, and T_3 positions to control the wind direction angle of 0°, 15°, and 30°. The x-direction is defined as the direction parallel to the span, the y-direction is defined as the out-of-plane direction, and the z-direction is defined as the vertical in-plane direction.

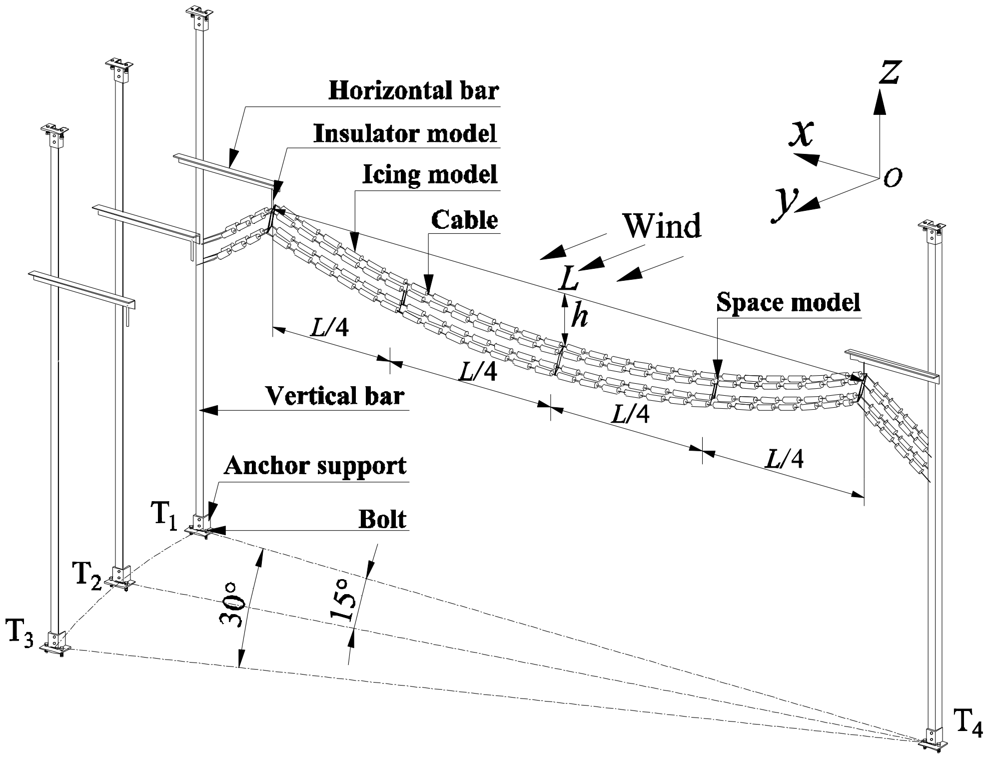

Figure 4. Design and installation schematic diagram of the aero-elastic model (unit: mm).

In the wind tunnel laboratory, the transmission line model is connected through the equivalent towers installed on both sides of the wind tunnel. Figure 4 shows the photos of the aero-elastic model and measurement equipment. The equivalent tower model was fixed on the upper and lower walls of the wind tunnel through the upper and lower anchors and bolts by friction and bolts. The tower and the line are connected with tension springs fixed by the iron transmission line to simulate the line insulator.

In the test, the influence of the flow direction (wind direction angle) on the galloping of the four-split ice-covered transmission line model was mainly considered. The wind speed increased from 3 m/s to 9 m/s with an interval of 1 m/s. There were different wind direction angles in the test. The test wind direction angles included 0°, 15°, and 30°. The change of different wind direction angles needs to be realized by moving one end of the transmission line to equalize the position of the tower. In addition, to realize the conversion of the vertical action and the oblique action of the wind load, one end of the equal tower was moved.

As shown in Figure 5, the displacement time histories of the ice-covered transmission line model was measured by a non-contact, multi-point laser displacement measurement equipment, which was placed outside the wind tunnel through the glass window. The in-plane and out-of-plane directions displacement time histories of seven displacement measuring points, which were labeled D_i (I = 1, 2, ... 7), were measured synchronously. Laser spot reflective papers were attached to the surface of the ice-covered transmission line models to ensure the accurate tracking and acquisition of the dynamic displacement of the model by the laser displacement measurement equipment. Among them, measuring points D_1, D_3, D_5, and D_7 were set at the middle of the ice segment models of the upper transmission line model; measuring points D_2, D_4, and D_6 were set at the middle of the side vertical bars of the spacer models. As shown in Figure 1 and Table 1, the span L, which is the horizontal distance between the hanging points at the both ends of the transmission line model, is 3.5 m. The height of the spacer, which is also the space between the transmission lines and the bundle, is 100 mm. The sag of the four-split transmission line model, which is the vertical distance between the middle of the side vertical bar of the spacer model at the middle span of the transmission line model to the mid-point of the line connected between the two hanging points at the both ends of the transmission line model, is 400 mm. The sampling frequency of the displacement measurement equipment was 119 Hz. The time histories of the wind-induced strains on the aluminum sheet suspended between the insulator model and the horizontal bar of the equivalent tower at the both sides of the wind tunnel were synchronously collected. The sampling frequency was 1024 Hz, and the measuring points were labeled as S_1 and S_2. The positive direction of the strain is set to be tensile strain. The wind speed time history was collected by a Cobra anemometer installed 3 m in front of the equivalent tower and at the same height as the hanging point of the iced transmission line model, and the sampling frequency was 1024 Hz.

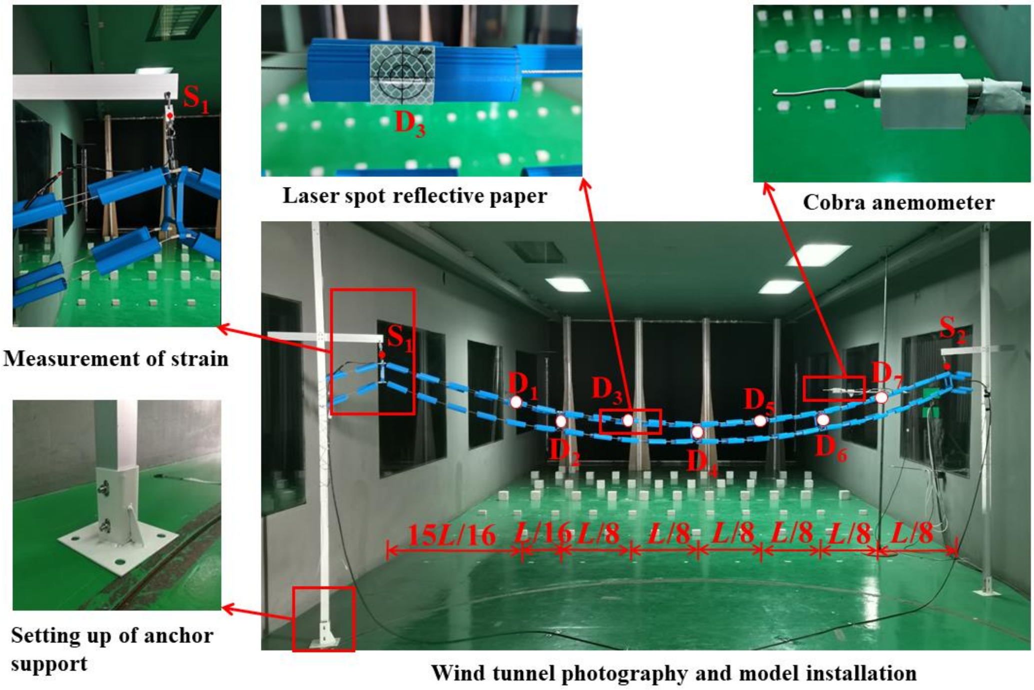

(**a**)

(**b**)

Figure 5. Photos of the aero-elastic model and measurement equipment: (**a**) setting up of the model. (**b**) Laser displacement measurement equipment.

The galloping of transmission lines is mostly observed in open terrain areas, and B-type terrain with a power index of 0.15 was simulated in the test by arranging rough elements in the wind tunnel laboratory. The laboratory wind field was verified before the test to check whether it meets the target landforms. The measurement was carried out before the tests, as shown in Figure 6. U_z and U_{ref} are the mean wind speed at height z and reference height, respectively. I_z is the turbulence intensity at height z, $S_u(f)$ is the power spectrum of wind velocity fluctuation, f is the frequency of the wind speed, L_u is the turbulence integral scale, and σ_u is the standard deviation of the wind speed U. The results show that the mean wind speed profile, turbulence intensity profile, and wind speed power spectrum simulated in the wind tunnel meet the requirements of the specification.

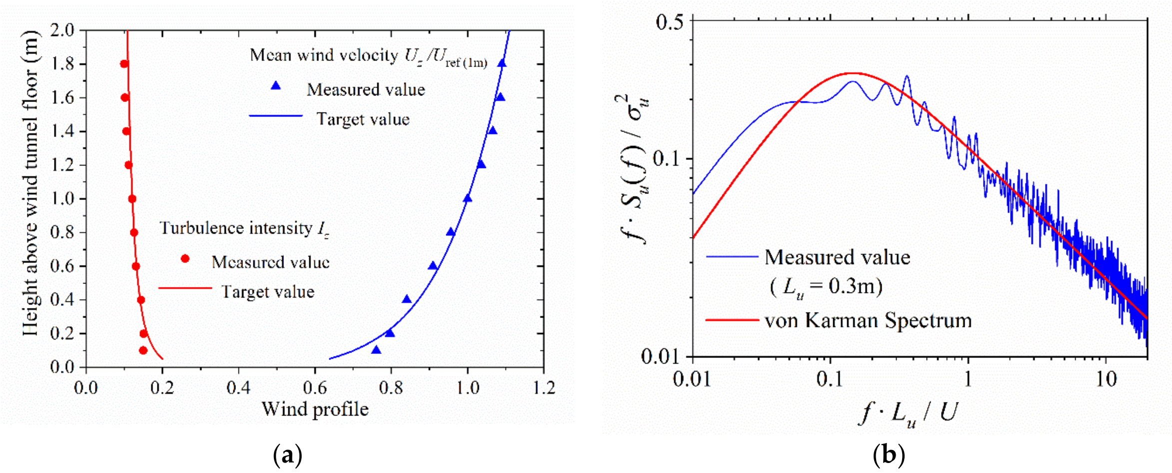

Figure 6. Atmospheric boundary layer simulation results. (**a**) Mean wind speed and turbulence intensity profiles; (**b**) Wind speed power spectrum.

2.2. Data Processing Methods

In the analysis of the results of the six-component force balance force measurement test, the overall drag, lift, and torsion coefficients of the four-split conductor are obtained by analyzing the force measurement results of the ice-covered sub-conductors. Subsequently, the coefficients are substituted into the galloping discriminant of Den Hartog and Nigel to determine the type of galloping.

In the force measurement wind tunnel test, the lift $F_{Li}(t)$ and drag $F_{Di}(t)$ of the ith ice-covered conductor model at time t under the incoming flow axis coordinate can be calculated using the following equation:

$$\begin{bmatrix} F_{Di}(t) \\ F_{Li}(t) \end{bmatrix} = \begin{bmatrix} cos\varphi & -sin\varphi \\ sin\varphi & cos\varphi \end{bmatrix} \begin{bmatrix} F_{xi}(t) \\ F_{yi}(t) \end{bmatrix} \quad (1)$$

where φ is the angle between the force balance coordinate axis and the incoming flow coordinate axis, and $F_{xi}(t)$ and $F_{yi}(t)$ represent the lift and drag of the ith ice-covered conductor under the axis coordinate of the six-component force balance at time t.

Then, the drag, lift, and torsion coefficients of the ith ice-covered conductor at time t can be calculated using the following equations:

$$C_{Di}(t) = \frac{F_{Di}(t)}{0.5\rho U^2 DH} \quad (2)$$

$$C_{Li}(t) = \frac{F_{Li}(t)}{0.5\rho U^2 DH} \quad (3)$$

$$C_{Mi}(t) = \frac{M_i(t)}{0.5\rho U^2 D^2 H} \quad (4)$$

where $C_{Di}(t)$, $C_{Li}(t)$, and $C_{Mi}(t)$ represent the drag, lift, and torsion coefficients of the ith (i = 1, 2, 3, 4) conductor at time t, respectively. $M_i(t)$ represents the torsion of the ith (i = 1, 2, 3, 4) conductor. ρ =1.225 kg/m^3 is the density of the air. U = 10 m/s is the mean value of the coming flow velocity. D is the overall diameter of the conductor plus ice, and H = 35 cm is the effective length of the ice-covered conductor model.

In order to study the variation law of the overall aerodynamic force of the four-split conductor with the wind attack angle, the mean values of the aerodynamic coefficients of four sub-conductors are used to represent the overall aerodynamic coefficients of the four-split conductor. The overall drag, lift, and torsion coefficients of the four-split conductor at time t are defined as:

$$C_D^N(t) = \frac{C_{D1}(t) + C_{D2}(t) + C_{D3}(t) + C_{D4}(t)}{N} \tag{5}$$

$$C_L^N(t) = \frac{C_{L1}(t) + C_{L2}(t) + C_{L3}(t) + C_{L4}(t)}{N} \tag{6}$$

where N is the number of sub-conductors in this study, N = 4.

The overall torsion coefficient of four-split conductor at time t is defined as:

$$C_M^N(t) = \frac{1}{N}(C_{M-D}(t) + C_{M-L}(t) + C_{M-m}(t)) \tag{7}$$

where $C_M^N(t)$ is the overall aerodynamic torsion coefficient of the four-split conductor; $C_{M-D}(t)$ represents the component of sub-conductor drag to the overall torsional force of the four-split conductor; $C_{M-L}(t)$ represents the component of sub-conductor lift to overall torsional force of four-split conductor; $C_{M-m}(t)$ represents the component of aerodynamic torsion of four-split conductor caused by self-torsion of sub conductor.

$C_{M-D}(t)$, $C_{M-L}(t)$ and $C_{M-m}(t)$ can be calculated using the following equations:

$$C_{M-D}(t) = \frac{1}{\sqrt{2}}\left[(C_{D1}(t) - C_{D3}(t))sin\left(\frac{\pi}{4} + \alpha\right) - (C_{D2}(t) - C_{D4}(t))cos\left(\frac{\pi}{4} + \alpha\right)\right] \tag{8}$$

$$C_{M-L}(t) = \frac{1}{\sqrt{2}}\left[(C_{L1}(t) - C_{L3}(t))sin\left(\frac{\pi}{4} + \alpha\right) - (C_{L2}(t) - C_{L4}(t))cos\left(\frac{\pi}{4} + \alpha\right)\right] \tag{9}$$

$$C_{M-m}(t) = \frac{D}{B}(C_{m1}(t) + C_{m2}(t) + C_{m3}(t) + C_{m4}(t)) \tag{10}$$

where i (i = 1, 2, 3, 4) represent the number of the sub-conductor. $C_{Di}(t)$, $C_{Li}(t)$, and $C_{mi}(t)$ represent the drag, lift and torsion coefficients of the ith ice-covered conductor, respectively. B is the distance from the center of the bundled conductor to the axis of the sub-conductor.

The overall drag, lift and torsion coefficients of the four-split conductor (C_D, C_L, and C_M) at each wind attack, can be obtained by averaging $C_D^N(t)$, $C_L^N(t)$, and $C_M^N(t)$.

In the vibration measurement wind tunnel tests, the wind-induced displacement and strain responses under different wind directions are investigated. The mean and standard deviation values of the response time histories are firstly analyzed. Furthermore, combined with power spectrum analysis, trajectory analysis, and damping ratio analysis is how the aero-elastic galloping characteristics were determined.

The mean and standard deviation values of the wind-induced response time histories are calculated by the following equations:

$$\overline{x} = \frac{x_{1+}x_{2+\ldots+}x_n}{n} \tag{11}$$

$$\overline{\sigma} = \sqrt{\frac{(x_1 - \overline{x})^2 + (x_2 - \overline{x})^2 + \ldots + (x_n - \overline{x})^2}{n-1}} \tag{12}$$

where x_i (I = 1, 2, . . . , n) is the ith sample of the wind-induced response time-histories, and n is the sampling length.

3. Aerodynamic Force Characteristics Analysis

3.1. Force Coefficients

The aerodynamic coefficients of each sub-conductor and four-split conductor can be calculated by Equations (1)–(10).

Figure 7 shows the aerodynamic coefficient results of each sub-conductor and four-split conductor changing with the wind angle of attack. It can be seen from Figure 7a–c that the aerodynamic coefficients of different sub-conductors, such as lift coefficient, drag coefficient, and torsion coefficient, share a similar tendency with regards to the wind attack angle, and their values are close. The lift coefficient has obvious peaks at 30°and 170° wind attack angles. The drag coefficient has an obvious peak value at 90° wind attack angle. The peak value of the torsion coefficient appears at the 40° wind attack angle.

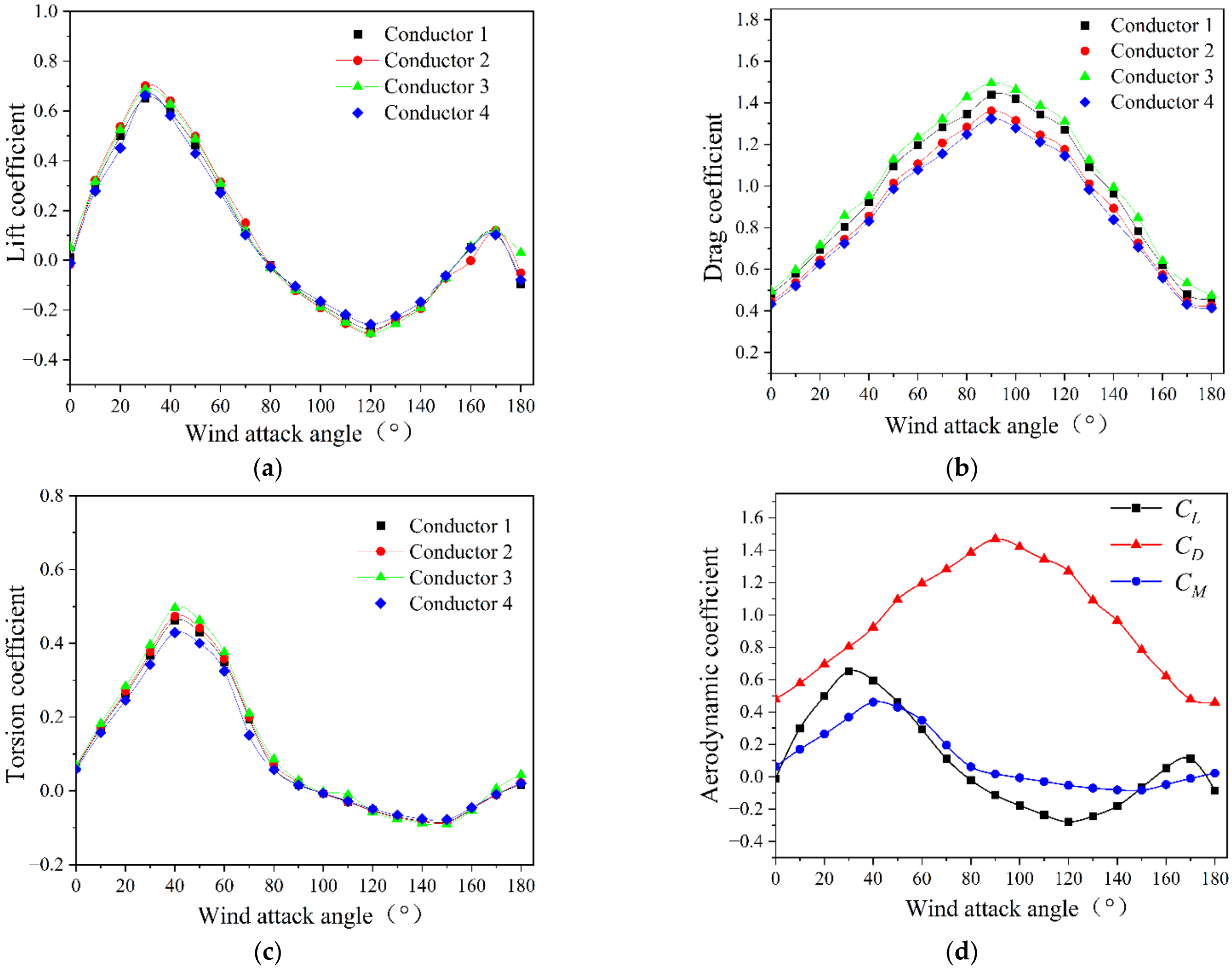

Figure 7. Curves of aerodynamic coefficients with wind attack angle: (**a**) Lift coefficient, (**b**) Drag coefficient, (**c**) Torsion coefficient, (**d**) Overall aerodynamic coefficient of four-split conductor.

By substituting the aerodynamic coefficient results of each sub-conductor at different wind attack angles into Equations (5) and (6), the overall aerodynamic coefficients of the four-split ice-covered conductor are obtained, as shown in Figure 7d.

3.2. Galloping Analysis Based on Den Hartog and Nigel's Theories

According to Den Hartog and Nigel's galloping theories, the discriminant of vertical galloping and torsion galloping for ice-coated conductor are shown as follows:

$$\varepsilon_{y,Den} = \frac{1}{8\pi}\rho UD\left(\frac{\partial C_L}{\partial \alpha} + C_D\right)\frac{1}{mf_y} \tag{13}$$

$$\varepsilon_{\theta,Nigel} = \frac{1}{8\pi}\rho URD^2\frac{\partial C_M}{\partial \alpha}\frac{1}{Jf_\theta} \tag{14}$$

where ρ is the air density, U is the wind speed, D is the diameter of the iced conductor, and R is the characteristic radius. C_L, C_D, and C_M are the mean value of $C_D^N(t)$, $C_L^N(t)$, and $C_M^N(t)$, f_y and f_θ are the vertical and torsional frequencies, m is the unit length mass of the iced conductor, and J is the moment of inertia per unit length.

In the above equations, only the lift-drag coefficient, torsion coefficient, and wind attack angle will affect the positive and negative damping ratio. After simplifications, the discriminant damping coefficients are defined as follows:

$$\varepsilon'_{y,\ Den} = \frac{\partial C_L}{\partial \alpha} + C_D \tag{15}$$

$$\varepsilon'_{\theta,Nigel} = \frac{\partial C_M}{\partial \alpha} \tag{16}$$

where $\varepsilon'_{y,\ Den}$ and $\varepsilon'_{\theta,Nigel}$ are the Den Hartog damping coefficient and the Nigel damping coefficient, respectively. When $\varepsilon'_{y,\ Den} \leq 0$, the four-split conductor gallops mainly due to vertical vibration, where when $\varepsilon'_{\theta,Nigel} \leq 0$, the four-split conductor gallops mainly due to torsional vibration.

Figure 8 shows the curves of Den Hartog and Nigel damping coefficients with the wind attack angle. It can be seen from the figure that Den Hartog coefficients are always positive, and the Nigel damping coefficients are negative in the range of 50° to 140° wind attack angle, that is, the four-split conductor will gallop mainly due to torsional vibration in this wind attack angle range. The galloping results from a combination of torsional and vertical motion of the bundle, which are coupled by the aerodynamic forces [42].

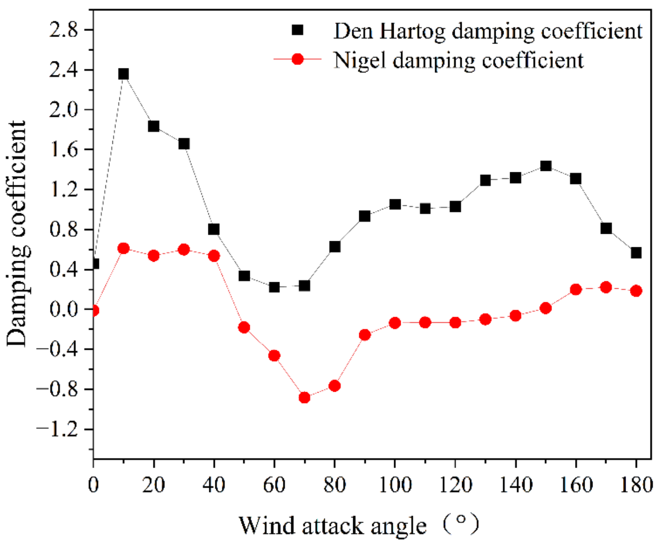

Figure 8. Den Hartog and Nigel damping coefficient.

In the aero-elastic model wind tunnel test, it is found that the ice-covered four-split transmission line model are usually within the wind attack angle range mentioned above.

4. Aero-Elastic Response Characteristics Analysis

In the six-component force test, only the influence of the wind attack angle change on the aerodynamic force of iced conductor can be considered. However, the influence of the flow direction (wind direction angle) on the overall response of four-split ice-covered transmission lines cannot be considered. In the aero-elastic model test, the influence of the wind direction angle change on the wind-induced vibration response of transmission lines was mainly studied. The wind direction angle diagram is shown in Figure 2. In the wind tunnel laboratory, the angle between the incoming flow and the axis of the four-split ice-covered conductor model was formed by moving the position of the equivalent tower. Three wind direction angles were considered: 0°, 15°, and 30°.

4.1. Statistical Characteristics

To study the influence of the wind direction angle on the aero-elastic response of the ice-covered transmission line model, the mean and standard deviation of in-plane and out-of-plane displacement time histories of measurement point D_4 (see Figure 3a) at 0°, 15°, and 30° wind direction angles were compared.

The mean and standard deviation values of the displacement of measurement point D_4 with various wind speeds are shown in Figure 9. It is observed that the mean and standard deviation values of displacement increase continuously with wind speed. The out-of-plane displacement are significantly larger than those of the in-plane displacement. As a result, the vibration process of the four-split ice-covered transmission line model is dominated by the out-of-plane vibration. The values under the oblique wind direction angles (15°, 30°) is obviously larger than 0° direct wind direction angle. The mean value of the displacement and standard deviation of in-plane vibration in the oblique wind direction are 1.3–1.5 times of 0° wind direction angle, and the out-of-plane vibration is 1.6–1.8 times. Conclusively, the transmission line is more prone to galloping at 15° and 30° wind direction angles, with larger galloping amplitude and lower critical wind speed.

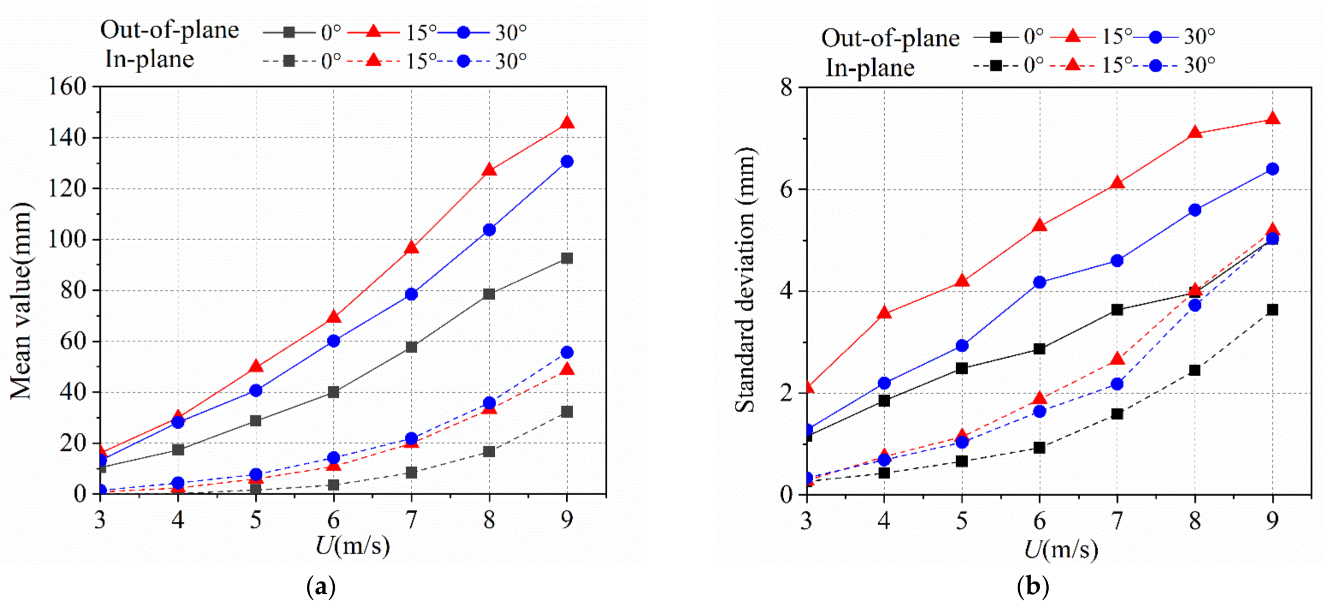

Figure 9. Mean and standard deviation values of displacement of measurement point D_4 with various wind speeds: (**a**) Mean values of displacement. (**b**) Standard deviation values of displacements.

It should be noted that the oscillation amplitudes obtained in the wind tunnel test are much lower than those experienced in a prototype scale because the weight of the icing model per unit length used in the experiment is much greater than the theoretical weight calculated according to the similarity theory.

4.2. Spectral Characteristics

The normalized power spectrum density (PSD) curves of measurement point D_4 at different wind direction angle were obtained through power spectrum analysis, which are shown in Figure 10. It can be seen that the first-order and third-order modes are mainly excited. According to the theory of in-plane and out-of-plane resonance of transmission lines, the lowest two in-plane and out-of-plane modes are not involved in an internal resonance with any of the other modes [43]. The out-of-plane vibration of the third-order mode may resonate with the in-plane vibration of the third-order mode at a frequency ratio of 1:1.

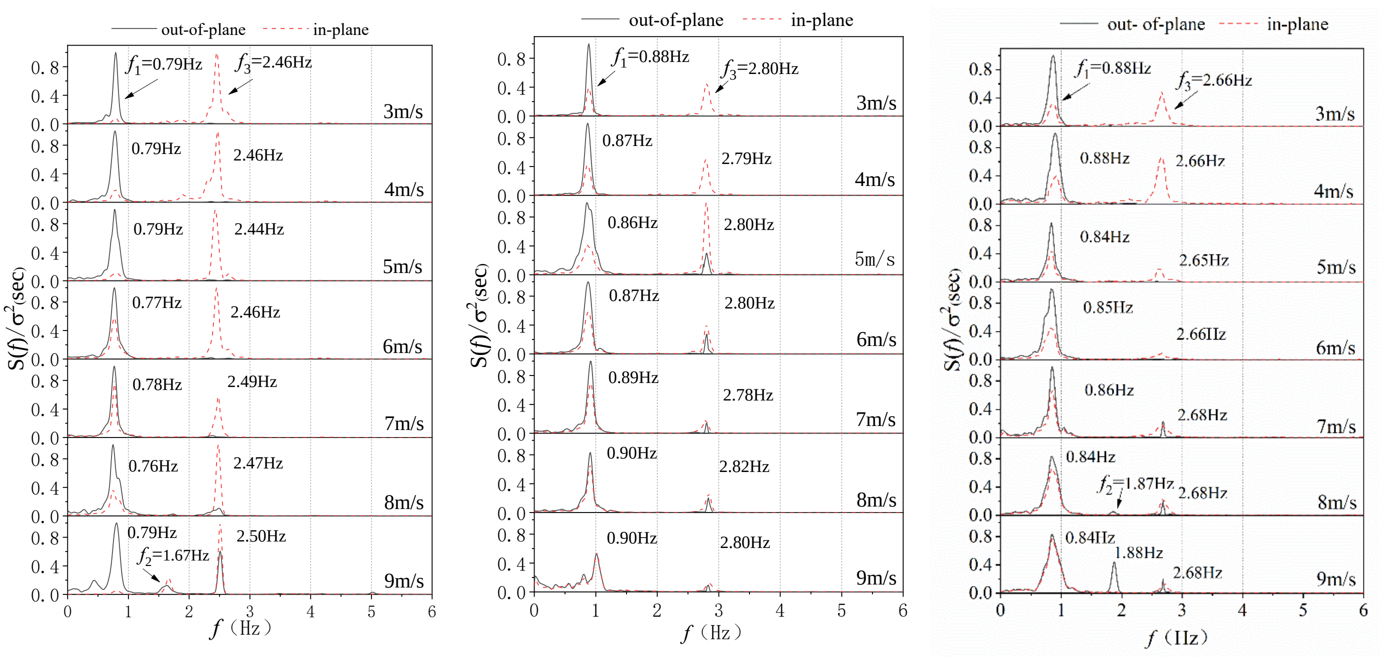

(**a**) (**b**) (**c**)

Figure 10. PSD of measuring point D_4 under oblique flows: (**a**) 0° wind direction, (**b**) 15° wind direction, (**c**) 30° wind direction.

At 0° wind direction angle, when the wind speed reaches 8m/s, the third-order mode of the 2.5 Hz frequency appears in the PSD curves of the in-plane and out-of-plane displacement. As a result, an in-plane and out-of-plane resonance with a frequency ratio of 1:1 may occur under these two cases. While at the wind direction angle of 15°, the in-plane and out-of-plane resonances with a frequency ratio of 1:1 dominated by third-order modes may occur at 5~9 m/s wind speed. This indicates that the in-plane and out-of-plane resonance with a frequency ratio of 1:1 dominated by the third-order mode is more likely to occur at a wind direction angle of 15°. When the wind direction angle is 30°, an in-plane and out-of-plane resonance with a frequency ratio of 1:1 may occur at 7 m/s, 8 m/s, and 9 m/s.

Figure 11 shows the normalized PSD curves of measurement point D_3 at different wind direction angles. The results show that under the same wind speed, the number of modes excited at different measuring points is different. In comparison, the number of modes excited at measuring point D_3 is more than that at measuring point D_4. The in-plane and out-of-plane vibration of the same order mode (modal order ≥ 2) will induce an internal resonance with a frequency ratio of 1:1 [44], resulting in a significant increase in the displacement response of the transmission line system compared with the case without coupling resonance.

According to Figures 10 and 11, it can be seen that under the same case, different orders and numbers of vibration modes are excited at different measuring points. This is because that when the displacement measuring point is located at the invariant node of a certain mode, the vibration amplitude of the measurement point is very small.

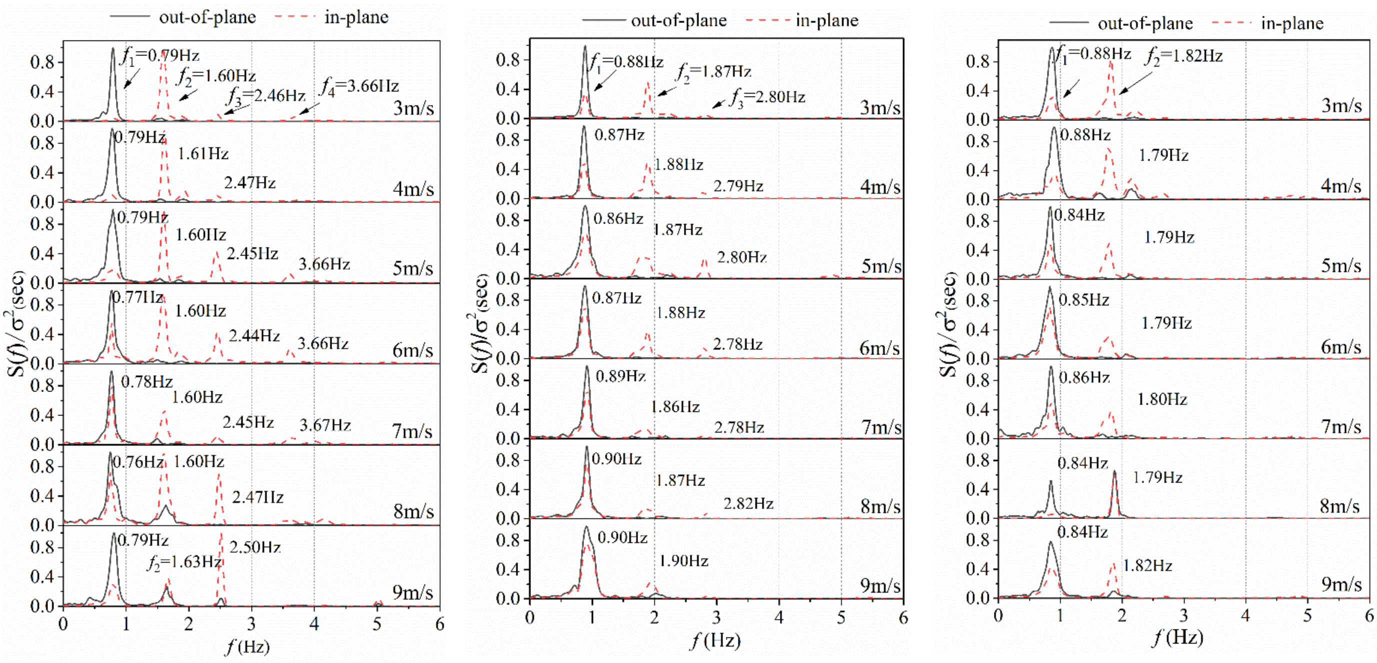

(a) (b) (c)

Figure 11. PSD of measuring point D_3 under oblique flows: (**a**) 0° wind direction, (**b**) 15° wind direction, (**c**) 30° wind direction.

Considering that the lowest two in-plane and out-of-plane modes are not involved in an internal resonance with any of the other modes [43]; while the number of wind speed conditions of the in-plane and out-of-plane modes excited at measuring point D_4 is much more than that of at measuring point D_3. Moreover, the vibration response of measuring point D_4 is significantly larger than that of other measuring points (D_4 is located at the mid-span position), the response of D_4 is selected as a representation in this study.

4.3. Trajectory Analysis

The elliptical trajectories of the displacement measurement point composed of in-plane and out-of-plane displacement time histories are often used to describe the spatial vibration characteristics of ice-covered conductors during galloping. When an elliptical trajectory is observed, it indicates that regular coupling occurs between the in-plane and out-of-plane modes. Combined with the PSD analysis results of the displacement time history in Section 4.2, the vibration trajectories of the in-plane and out-of-plane displacement time histories of measurement point D_4 are analyzed in this section. The results are shown in Figure 12.

It is observed from Figure 12 that compared with other wind speeds, the elliptical trajectory diameter at the 0° wind direction angle is larger at 8 m/s and 9 m/s wind speeds. This result is similar to the estimation of the third-order modal in-plane and out-of-plane coupling vibration at the 8 m/s and 9 m/s wind speeds obtained from the power spectrum analysis in Figure 10. At the 15° wind direction angle, no obvious elliptical trajectory is formed at the 3 m/s and 4 m/s wind speeds. After exceeding 5 m/s, the elliptical trajectory of the in-plane and out-of-plane displacement time history becomes increasingly obvious. Combined with the power spectrum analysis results, it can be seen that the excitation of the third-order mode in the out-of-plane vibration may be the reason for the occurrence of the in-plane and out-of-plane coupling vibration. Therefore, in comparison, the third-order mode of out-of-plane vibration is more prone to be excited at 15° wind direction angle, which leads to the coupling vibration of in-plane and out-of-plane vibration at lower wind speed. After the wind speed exceeds 5 m/s, the mean and standard deviation values of displacement are significantly larger than other wind directions.

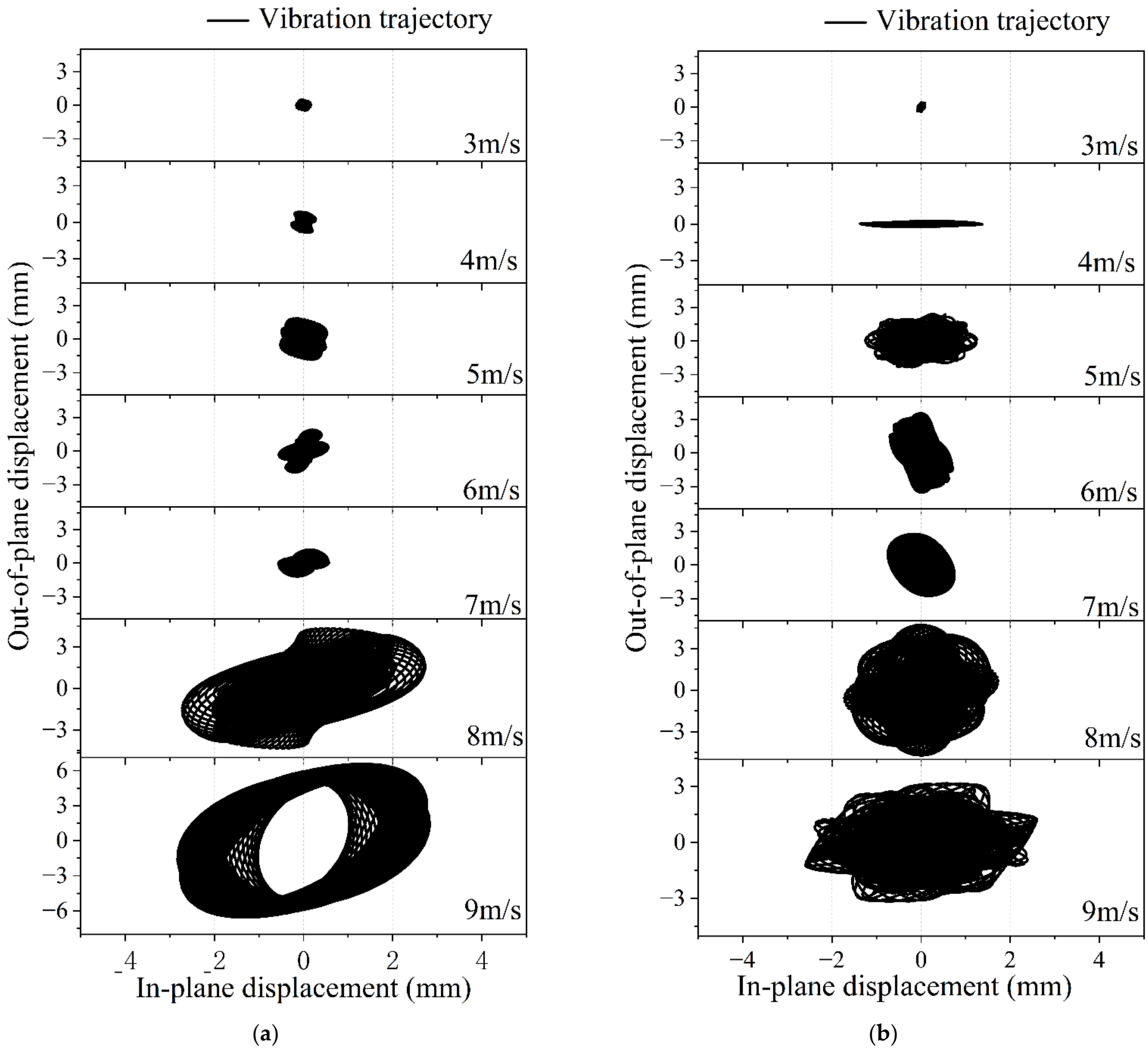

Figure 12. Vibration trajectories of out-of-plane and in-plane displacement time history of the third-order modal under different wind direction angles: (**a**) 0° wind direction angle. (**b**) 15° wind direction angle.

4.4. Correlation Analysis

A correlation coefficient is defined to analyze the correlation of in-plane and out-of-plane vibration responses.

$$\rho_{in,out} = \frac{\sum \left(D_{i,in}(t) - \overline{D_{i,in}}\right)\left(D_{i,out}(t) - \overline{D_{i,out}}\right)}{\sqrt{\sum \left(D_{i,in}(t) - \overline{D_{i,in}}\right)^2 \left(D_{i,out}(t) - \overline{D_{i,out}}\right)}} \tag{17}$$

where $\rho_{in,out}$ is the correlation coefficient of the in-plane and out-of-plane displacements, $D_{i,in}(t)$ and $D_{i,out}(t)$ are the in-plane and out-of-plane displacements of measurement point D_i at time t, respectively. $\overline{D_{i,in}}$ and $\overline{D_{i,out}}$ are the mean values of the in-plane and out-of-plane displacements of measurement point D_i, respectively.

Figure 13 shows the correlation coefficients of the in-plane and out-of-plane displacements of measurement point D_4 at different wind attack angles. The displacement time histories used in the analysis are the total displacement time histories of the measuring point. The results show that the correlation coefficients of in-plane displacement and out-of-plane displacement at the 15° wind direction angle and 30° wind direction angle are larger than those at the 0° wind direction angle under most wind speeds. It should be noted that, in this test, the vibrations under all cases are multi-mode combined vibrations, that is, there is no galloping in which a certain mode is absolutely dominant. Therefore, there is no correlation coefficient equals to 1.

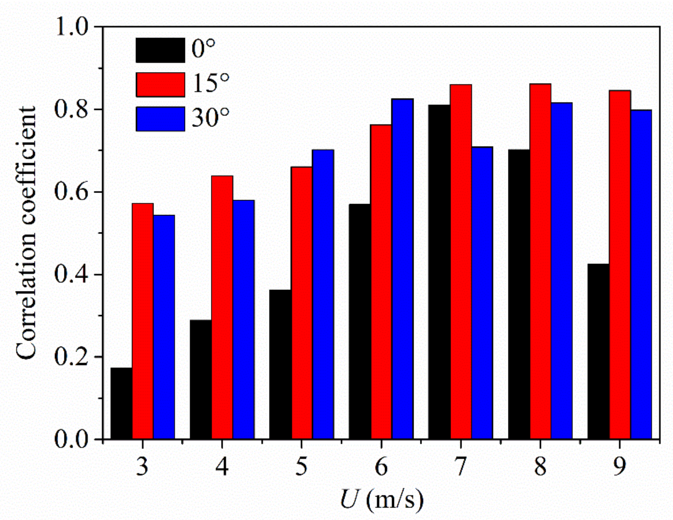

Figure 13. Correlation coefficients of the in-plane and out-of-plane displacements of measurement point D_4 at different wind attack angles.

4.5. Damping Ratio Analysis

It is generally believed that when the iced conductor is galloping, the damping ratio of the galloping mode is no more than 0. Therefore, the damping ratio of each order modal of displacement time history is often used to determine whether the transmission line is galloping.

Using the random decrement technique (RDT) [45,46], the damping ratios of the conductor are identified based on the displacement time history of the measurement point D_4. The analysis process is described as follows. Firstly, the power spectrum analysis of the displacement time history is carried out to obtain the power spectrum and the excited modal frequency value in the displacement response. Then, the modal displacement time history of each order is obtained by the band-pass filtering method. Subsequently, the RDT curve of each order modal displacement time history is obtained using the RDT method, and the damping ratio is solved by Hilbert transformation method.

Tables 2–4 shows the summary of the out-of-plane vibration and in-plane vibration damping ratios calculated for different wind direction angles for measuring point D_4. Negative damping ratios are highlighted in the tables.

According to the above damping ratio results, it can be seen that the negative damping occurs more frequently in the oblique wind direction (15° and 30°) than in the 0° wind direction angle, and the wind speed is lower. The negative damping at the 0° wind direction angle only occurs at wind speeds of 8 m/s and 9 m/s. However, negative damping occurs at wind speeds of 5 m/s and above when the oblique wind direction is 15°. In addition, negative damping occurs between 7 m/s and 9 m/s at a wind direction angle of 30°. When the negative damping appears, it corresponds to the phenomenon that the accompanying displacement gradually diverges in the mode. Figure 14 shows an example of negative RDT curves of the third-order modal displacement for measurement point D_4 at the 15° wind direction when the wind speed is 6 m/s. It can be seen that the vibration amplitude of the transmission line gradually increases within a certain period of time.

Table 2. Damping ratios recognized at 0° wind direction angle (%).

Wind Speed (m/s)	First-Order Out-of-Plane	First-Order in-Plane	Third-Order Out-of-Plane	Third-Order in-Plane
3 m/s	1.20	0.70	0.71	0.15
4 m/s	2.07	1.67	1.40	0.21
5 m/s	1.30	1.32	0.78	0.15
6 m/s	1.12	2.44	0.68	0.17
7 m/s	2.29	2.33	0.63	0.25
8 m/s	4.66	5.26	−0.07	−0.03
9 m/s	1.09	2.61	−0.06	−0.01

Table 3. Damping ratios recognized at 15° wind direction angle (%).

Wind Speed (m/s)	First-Order Out-of-Plane	First-Order in-Plane	Third-Order Out-of-Plane	Third-Order in-Plane
3 m/s	1.46	0.55	0.23	0.22
4 m/s	0.55	1.81	1.40	0.16
5 m/s	1.62	3.28	−0.33	−0.16
6 m/s	2.45	3.05	−0.19	−0.12
7 m/s	1.25	3.04	−0.50	−0.20
8 m/s	3.44	3.10	−0.39	−0.42
9 m/s	2.19	1.84	−0.50	−0.18

Table 4. Damping ratios recognized at 30° wind direction angle (%).

Wind Speed (m/s)	First-Order Out-of-Plane	First-Order in-Plane	Third-Order Out-of-Plane	Third-Order in-Plane
3 m/s	0.98	0.41	—	0.22
4 m/s	0.82	0.80	—	0.16
5 m/s	0.76	0.12	—	0.16
6 m/s	0.21	0.53	—	0.12
7 m/s	0.10	0.02	−0.10	−0.20
8 m/s	0.88	0.01	−0.16	−0.42
9 m/s	0.44	0.03	−0.03	−0.18

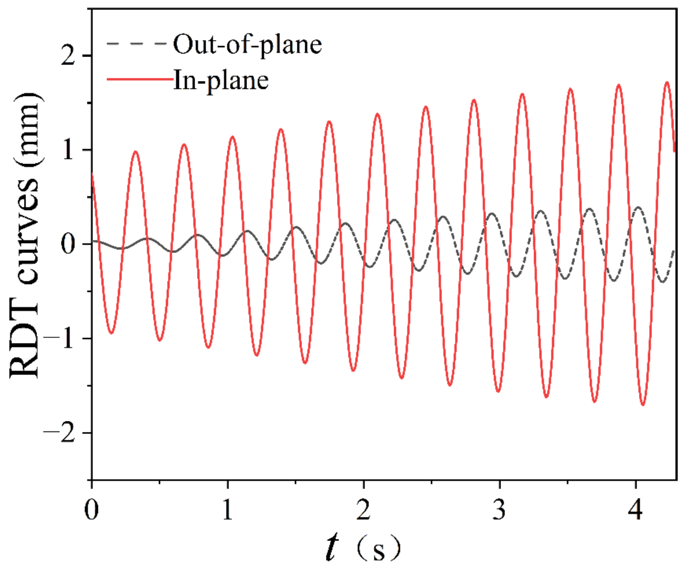

Figure 14. RDT curves example of the third-order modal displacement for measurement point D_4 at 15° wind direction when the wind speed is 6 m/s.

4.6. Wind-Induced Strain of the Equivalent Tower

When the galloping of the ice-covered four-split transmission line model occurs, the lift force on the iced transmission line model will significantly increase. When the lift is greater than the gravity, the mean value of the strain for the measurement point on the aluminum sheet, connected under the suspension points on both sides of the equivalent tower, will change from positive to negative. Therefore, the change of mean strain represents the change of lift.

In this section, the wind-induced strain of the equivalent tower is studied to further determine whether the ice-covered conductor model gallops. The strain gauge position and number are shown in Figure 5.

Figure 15 shows the time history of strain at measuring point S_1 with different wind speeds under the 15° wind direction angle. Table 5 shows the mean value of the strain for point S_1 with respect to the wind speed. It can be observed that the critical wind speed recognized by strain varying from positive to negative is completely consistent with the galloping critical wind speed obtained by the above-mentioned power spectrum analysis, trajectory analysis, and damping ratio analysis. The sign change of mean strain also represents the sudden increment of lift. Consequently, the lift of the iced four-split transmission line model at the 15° wind direction angle is generally larger than 30° and 0°, subsequently.

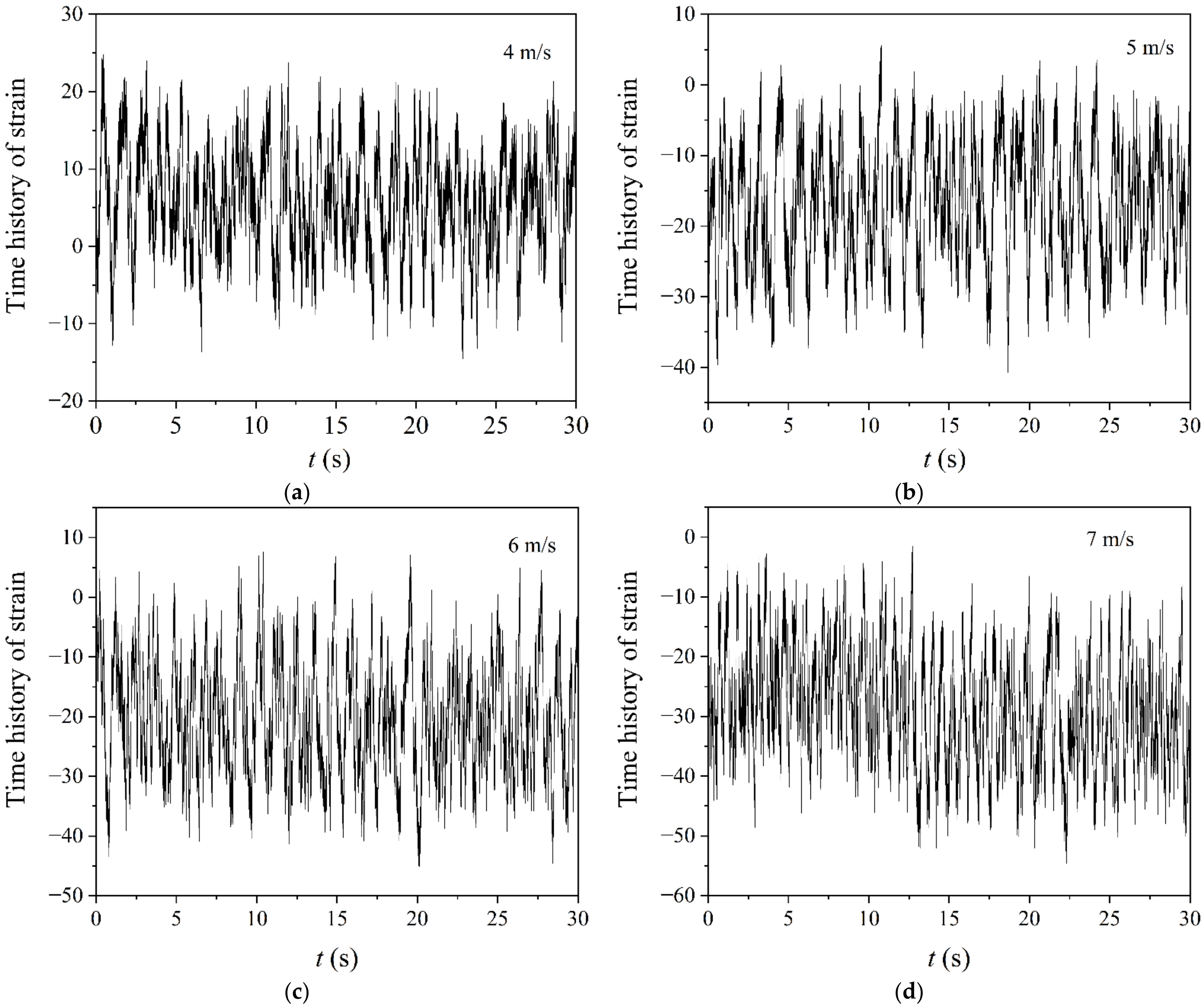

Figure 15. *Cont.*

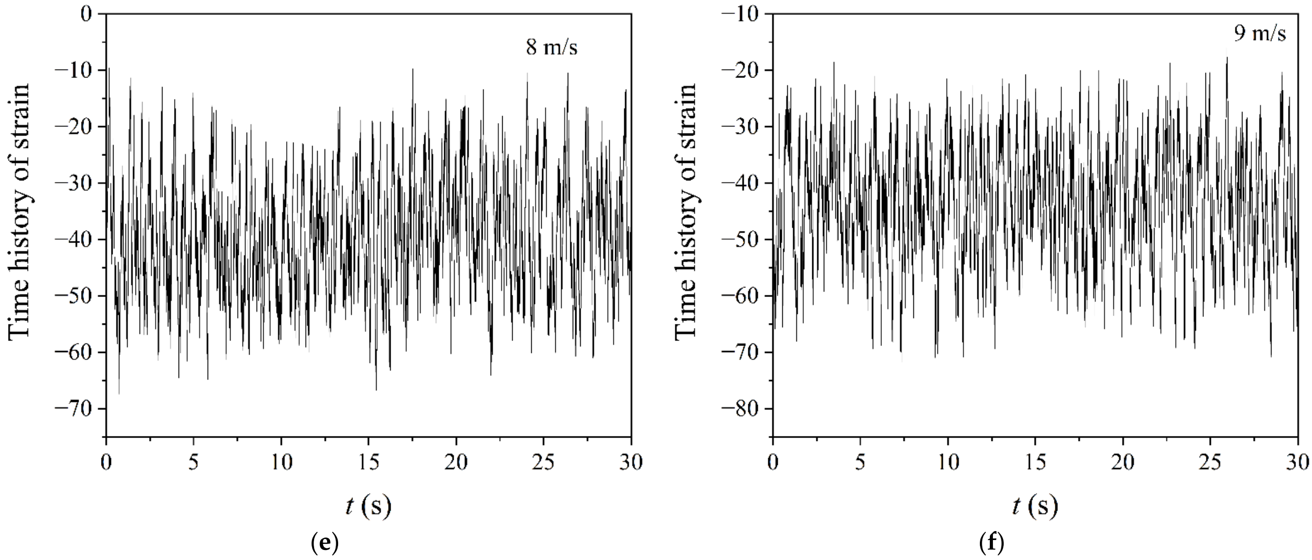

Figure 15. The time history of strain for measuring point S_1 at different wind speeds: (**a**) 4 m/s, (**b**) 5 m/s, (**c**) 6 m/s, (**d**) 7 m/€, (**e**) 8 m/s, (**f**) 9 m/s.

Table 5. Mean values of the strain ($\mu\varepsilon$) for strain measurement point S_1 changing with the wind speed at each wind direction angle.

Wind Speed (m/s)	Wind Direction Angle		
	0°	15°	30°
0	0.07	0.21	0.14
3	22.12	9.44	11.54
4	20.20	5.94	4.09
5	11.91	−16.88	7.94
6	10.36	−20.34	0.29
7	4.66	−28.48	−2.38
8	−0.28	−39.13	−13.54
9	−1.62	−43.50	−16.15

5. Conclusions

Through wind tunnel tests on the rigid and aero-elastic models of four-split ice-covered transmission line with crescent shape, the aerodynamic force and aero-elastic response characteristics are studied and the following concluding remarks are drawn.

(1) Based on the aerodynamic force measurement data, the galloping type of the crescent-shaped ice-covered four-split conductor used in this study belongs to torsional galloping, according to Nigel's damping coefficient criterion. While, Den Hartog coefficients are always positive, vertical galloping does not occur.

(2) According to the aero-elastic model test, the ice-covered four-split transmission line is more prone to galloping under oblique flows. The mean and standard deviation values of the galloping displacement at 15° > 30° > 0° wind direction angles.

(3) The mean and standard deviation values of the out-of-plane displacement of ice-covered four-split transmission lines are always larger than those of in-plane displacement. The in-plane response of the third-order mode is excited at all wind speeds. When the out-of-plane response of the third-order mode is excited, the four-split transmission line gallops. Moreover, the in-plane and out-of-plane displacement of the third-order mode resonance with a frequency ratio of 1:1, and the in-plane and out-of-plane displacement time history shows obvious elliptical trajectories. The damping ratios of the in-plane and out-of-plane displacements of the galloping mode are negative, the overall lift of the ice-covered four-split transmission line model increases substantially, and the strain changes from the positive to negative.

(4) The galloping of four-split ice-covered transmission lines is more prone to occur under oblique flows at the 15° and 30° wind direction angles, with larger galloping amplitude and lower critical wind speed. In this experimental study, whether galloping occurs has a significant relationship with whether the third-order mode of out-of-plane vibration is excited. At the 15° wind direction angle, after reaching 5 m/s wind speed, the out-of-plane vibration of the third-order mode is excited, and the in-plane and out-of-plane resonance vibration with a frequency ratio of 1:1 occurs. At the 30° wind direction, the in-plane and out-of-plane resonance of the third-order mode can be excited only when the wind speed reaches 7 m/s. At the 0° wind direction angle, it is necessary to reach 8 m/s wind speed, and the in-plane and out-of-plane resonance vibration of the third-order mode can be excited.

Author Contributions: Conceptualization, Z.C. and N.S.; methodology, Z.C. and N.S.; data curation, J.S. and W.C.; software, W.C. and J.S.; validation, Z.C., N.S. and B.N.; formal analysis, B.N.; investigation, W.C.; resources, Z.C.; writing—original draft preparation, W.C.; writing—review and editing, B.N.; visualization, C.Z.; supervision, Z.C.; project administration, Z.C.; funding acquisition, Z.C. All authors have read and agreed to the published version of the manuscript.

Funding: The work described in this paper is grateful to the financial support of the Key Research and Development Plan of Jilin Science and Technology Department (20210203165SF).

Institutional Review Board Statement: Not applicable.

Informed Consent Statement: Not applicable.

Data Availability Statement: The data, models, and code generated or used during the study are available from the fist author by reasonable request.

Conflicts of Interest: The authors declare no conflict of interest.

Abbreviations

Notation	**Description**
Ø	the diameter of the circle
F_L	the lift force of the ice-covered conductor model
F_D	the drag force of the ice-covered conductor
F_x	the force along the x axis of the six-component force balance
F_y	the force along the y axis of the six-component force balance
F_z	the force along the z axis of the six-component force balance
M_x	the moment along the x axis of the six-component force balance
M_y	the moment along the y axis of the six-component force balance
M_z	the moment along the z axis of the six-component force balance
α	the wind attack angle
λ_L	the geometric scale ratio
λ_U	the wind speed ratio
L	the span of the transmission line
T_i	the location of the *i*th equivalent tower (i = 1, 2, 3, 4)
D_i	the *i*th displacement measuring point (i = 1, 2, 3, 4, 5, 6, 7)
S_i	the *i*th measuring point of the wind-induced strain (i = 1, 2)
U_z	the mean wind speed at height z
U_{ref}	the mean wind speed at reference height
I_z	the turbulence intensity at height z
$S_u(f)$	the power spectrum of wind velocity fluctuation
f	the frequency
L_u	the turbulence integral scale
σ_u	the standard deviation of the wind speed
$F_{Li}(t)$	the lift force of the *i*th (i = 1, 2, 3, 4) ice-covered conductor model at time t
$F_{Di}(t)$	the drag force of the *i*th (i = 1, 2, 3, 4) ice-covered conductor model at time t
φ	the angle between the force balance coordinate axis and the incoming flow coordinate axis
$F_{xi}(t)$	the lift force of the *i*th (i = 1, 2, 3, 4) ice-covered conductor under the axis coordinate of the six-component force balance at time t

Notation	Description
$F_{yi}(t)$	the drag force of the ith (i = 1, 2, 3, 4) ice-covered conductor under the axis coordinate of the six-component force balance at time t
$C_{Di}(t)$	the drag coefficient of the ith (i = 1, 2, 3, 4) ice-covered conductor at time t
$C_{Li}(t)$	the lift coefficient of the ith (i = 1, 2, 3, 4) ice-covered conductor at time t
$C_{Mi}(t)$	the torsion coefficient of the ith (i = 1, 2, 3, 4) ice-covered conductor at time t
U	the wind speed
ρ	the density of air
$M_i(t)$	the torsion of the ith (i = 1, 2, 3, 4) conductor at time t
D	the overall diameter of the conductor covered with ice
H	the effective length of the ice-covered conductor model
$C_D^N(t)$	the overall drag coefficient of the four-split conductor at time t
$C_L^N(t)$	the overall lift coefficient of the four-split conductor at time t
$C_M^N(t)$	the overall torsion coefficient of the four-split conductor at time t
N	the number of sub-conductors
$C_{M-D}(t)$	the component of sub-conductor drag to overall torsional force of four-split conductor
$C_{M-L}(t)$	the component of sub-conductor lift to overall torsional force of four-split conductor
$C_{M-m}(t)$	the component of aerodynamic torsion of four-split conductor caused by self-torsion of sub conductor
B	the distance from the center of the bundled conductor to the axis of the sub-conductor
C_D	the overall drag coefficient of the four-split conductor
C_L	the overall lift coefficient of the four-split conductor
C_M	the overall torsion coefficient of the four-split conductor
$\overline{x}$	the mean value of response time history
$\overline{\sigma}$	the standard deviation value of response time history
x_i	the ith sample of the wind-induced response
n	the sampling length of the wind-induced response
$\varepsilon_{y,Den}$	the discriminant of vertical galloping
$\varepsilon_{\theta,Nigel}$	the discriminant of torsion galloping
R	the characteristic radius
f_y	the vertical frequency of the transmission line without wind
f_θ	the torsional frequency of the transmission line without wind
m	the unit length mass of the iced conductor
J	the moment of inertia per unit length
$\varepsilon'_{y,\ Den}$	Den Hartog damping coefficient
$\varepsilon'_{\theta,Nigel}$	Nigel damping coefficient
$\rho_{in,out}$	the correlation coefficient of in-plane and out-of-plane displacements
$D_{i,in}(t)$	the in-plane displacement of measurement point D_i at time t
$D_{i,out}(t)$	the out-of-plane displacement of measurement point D_i at time t
$\overline{D_{i,in}}$	the mean values of the in-plane displacement of measurement point D_i
$\overline{D_{i,out}}$	the mean values of the out-of-plane displacements of measurement point D_i

References

1. Dyke, P.V.; Laneville, A. Galloping of a Single Conductor Covered with a D-Section on a High-Voltage Overhead Test Line. *J. Wind Eng. Ind. Aerodyn.* **2008**, *96*, 1141–1151. [CrossRef]
2. Hung, P.V.; Yamaguchi, H.; Isozaki, M.; Gull, J.H. Large Amplitude Vibrations of Long-Span Transmission Lines with Bundled Conductors in Gusty Wind. *J. Wind Eng. Ind. Aerodyn.* **2014**, *126*, 48–59. [CrossRef]
3. Gurung, C.B.; Yamaguchi, H.; Yukino, T. Identification and Characterization of Galloping of Tsuruga Test Line Based on Multi-Channel Modal Analysis of Field Data. *J. Wind Eng. Ind. Aerodyn.* **2003**, *91*, 903–924. [CrossRef]
4. Gao, Y.; Yang, J.; Zhang, K.; Peng, H.; Wang, Y.; Xia, N.; Yao, G. A New Method of Conductor Galloping Monitoring Using the Target Detection of Infrared Source. *Electronics* **2022**, *11*, 1207. [CrossRef]
5. Wang, L.; Li, H.; Lu, X.; Li, X.; Zhang, J.; Wang, X.; Chen, C. Design of Intelligent Monitoring System in Galloping Power Transmission Line. *Sensors* **2022**, *22*, 4197. [CrossRef]
6. Chen, W.; Li, Y.; Zhao, Z. Transmission Line Vibration Damper Detection Using Deep Neural Networks Based on UAV Remote Sensing Image. *Sensor.* **2022**, *22*, 1892. [CrossRef]
7. Li, G.; Li, L.; Zhu, P. Galloping Control for Iced Conductors Using Tuned Mass Dampers with Fixed Time-Delayed Feedback. *Shock Vib.* **2019**, *2019*, 4823457. [CrossRef]
8. DenHartog, J.P. Transmission Line Vibration Due to Sleet. *T. Am. Inst. Electr. Eng.* **1932**, *51*, 1074–1076. [CrossRef]

9. Nigol, O.; Buchan, P.G. Conductor Galloping Part I-Den Hartog Mechanism. *IEEE Trans. Power Syst.* **1981**, *PAS-100*, 699–707. [CrossRef]
10. Yu, P.; Popplewell, N.; Shah, A.H. Instability Trends of Inertially Coupled Galloping. Part I: Initiation. *J. Sound Vib.* **1995**, *183*, 663–678. [CrossRef]
11. Yu, P.; Popplewell, N.; Shah, A.H. Instability Trends of Inertially Coupled Galloping. Part II: Initiation. *J. Sound Vib.* **1995**, *183*, 679–691. [CrossRef]
12. Guo, P.; Wang, D.W.; Li, S.; Liu, L.L.; Wang, X.D. Transiting Test Method for Galloping of Iced Conductor Using Wind Generated by a Moving Vehicle. *Wind Struct.* **2019**, *28*, 155–170. [CrossRef]
13. Guo, P.; Li, S.; Wang, D.W. Analysis of Wind Attack Angle Increments in Wind Tunnel Tests for the Aerodynamic Coefficients of Iced Hangers. *Adv Struct Eng.* **2019**, *23*, 603–613. [CrossRef]
14. Lou, W.J.; Wu, D.G.; Xu, H.W.; Yu, J. Galloping Stability Criterion for 3-DOF Coupled Motion of an Ice-Accreted Conductor. *J. Struct. Eng.* **2020**, *146*, 04020071. [CrossRef]
15. Wen, Z.P.; Xu, H.W.; Lou, W.J. Eccentricity-Induced Galloping Mechanism of a Vertical-Torsional Coupled 3-DOF System. *J. Wind. Eng. Ind. Aerod.* **2022**, *229*, 105174. [CrossRef]
16. Lou, W.J.; Huang, C.R.; Huang, M.F.; Yu, J. An Aerodynamic Anti-Galloping Technique of Iced 8-Bundled Conductors Inltra-High-Voltage Transmission Lines. *J. Wind. Eng. Ind. Aerod.* **2019**, *193*, 103972. [CrossRef]
17. Xie, Q.; Qi, G.S.; Zheng, G.; Yong, Z. Wind Tunnel Test on Global Drag Coefficients of Multi-Bundled Conductors. *J. Wind Eng. Ind. Aerodyn.* **2013**, *120*, 9–18. [CrossRef]
18. Huang, G.Z.; Yan, B.; Liu, J.Q.; Wu, C.; Lv, Z.B. Experimental Study on Torsional Behavior of Twin Bundle Conductor lines. *IEEE Trans. Power Deliv.* **2020**, *35*, 1423–1431. [CrossRef]
19. Chabart, O.; Lilien, J.L. Galloping of Electrical Lines in Wind Tunnel Facilities. *J. Wind. Eng. Ind. Aerod.* **1998**, *74*, 967–976. [CrossRef]
20. Zdero, R.; Turan, O.F. The Effect of Surface Strands, Angle of Attack, and Ice Accretion on the Flow Field Around Electrical Power Cables. *J. Wind. Eng. Ind. Aerod.* **2010**, *98*, 672–678. [CrossRef]
21. Li, X.M.; Nie, X.C.; Zhu, Y.K.; You, Y.; Yan, Z.T. Wind Tunnel Tests on Aerodynamic Characteristics of Ice-Coated 4-Bundled Conductors. *Math. Probl. Eng.* **2017**, *2017*, 1628173. [CrossRef]
22. Zhou, L.S.; Yan, B.; Zhang, L.; Zhou, S. Study on Galloping Behavior of Iced Eight Bundle Conductor Transmission Lines. *J. Sound Vib.* **2016**, *362*, 85–110. [CrossRef]
23. Bartoli, G.; Cluni, F.; Gusella, V.; Procino, L. Dynamics of Cable under Wind Action: Wind Tunnel Experimental Analysis. *J. Wind. Eng. Ind. Aerod.* **2006**, *94*, 259–273. [CrossRef]
24. Rega, G.; Tayor, C.A. dynamics of cable stays. Part 1: Sinusoidal cable support excitation. *J. Sound Vib.* **2005**, *281*, 537–564. [CrossRef]
25. Rega, G.; Warminski, J. Theoretical and Experimental Nonlinear Vibrations of Sagged Elastic Cables. *Solid Mech. Its Appl.* **2012**, *181*, 159–210. [CrossRef]
26. Benedettini, F.; Rega, G.; Alaggio, R. Non-Linear Oscillations of a Four-Degree-of-Freedom Model of a Suspended Cable under Multiple Internal Resonance Conditions. *J. Sound Vib.* **1995**, *182*, 775–798. [CrossRef]
27. Liu, X.H.; Huo, B. Nonlinear Vibration and Multimodal Interaction Analysis of Transmission Line with Thin Ice Accretions. *Int. J. Appl. Mech.* **2015**, *7*, 1540007. [CrossRef]
28. Liu, X.H.; Yang, S.; Wu, C.; Zou, M.; Min, G.; Sun, C.; Cai, M. Planar Nonlinear Galloping of Iced Transmission Lines under Forced Self-Excitation Conditions. *Discrete Dyn. Nat. Soc.* **2021**, *2021*, 6686028. [CrossRef]
29. Liu, X.H.; Yang, S.H.; Min, G.H.; Cai, M.H.; Wu, C.H.; Jiang, Y. Investigation on the Accuracy of Approximate Solutions Obtained by Perturbation Method for Galloping Equation of Iced Transmission Lines. *Math. Probl. Eng.* **2021**, *2021*, 6651629. [CrossRef]
30. Nino, S.D.; Luongo, A. Nonlinear Aero-elastic in-Plane Behavior of Suspension Bridges under Steady Wind Flow. *Appl. Sci.* **2020**, *10*, 1689. [CrossRef]
31. Ferretti, M.; Zulli, D.; Luongo, A. A Continuum Approach to the Nonlinear In-Plane Galloping of Shallow Flexible Cables. *Adv. Math Phys.* **2019**, *2019*, 6865730. [CrossRef]
32. Nie, X.C.; Pei, S.; Tan, T.; Yan, Z.T.; Yan, Z.M. Nonlinear 1:2 Internal Resonance Response of L-Shaped Piezoelectric Energy Harvester under the Influence of Electrical Damping. *Int. J. Mech. Sci.* **2022**, *225*, 107365. [CrossRef]
33. Nie, X.C.; Gao, X.; Wang, L.; Tan, T.; Yan, Z.T.; Yan, Z.M.; Liu, X. Nonlinear Analysis of the Internal Resonance Response of an L-Shaped Beam Structure Considering Quadratic and Cubic Nonlinearity. *J. Stat. Mech. Theory Exp.* **2022**, *2022*, 023204. [CrossRef]
34. Yan, Z.T.; Li, Z.L.; Savory, E.; William, E.L. Galloping of a Single Iced Conductor Based on Curved-Beam Theory. *J. Wind Eng. Ind. Aerodyn.* **2013**, *123*, 77–87. [CrossRef]
35. Yan, Z.T.; Savory, E.; Li, Z.L.; William, E.L. Galloping of Iced Quad-Conductor Bundles Based on Curved Beam Theory. *J. Sound Vib.* **2014**, *333*, 1657–1670. [CrossRef]
36. Wu, C.; Yan, B.; Huang, G.Z.; Zhang, B.; Lv, Z.B.; Li, Q. Wake-Induced Oscillation Behaviour of Twin Bundle Conductor Transmission Lines. *Roy. Soc. Open Sci.* **2018**, *5*, 180011. [CrossRef]
37. Liao, P.; Fu, J.; Ma, W.; Cai, Y.; He, Y. Study on the Efficiency and Dynamic Characteristics of an Energy Harvester Based on Flexible Structure Galloping. *Energies* **2021**, *14*, 6548. [CrossRef]

38. Ding, L.; Zou, Q.; Zhang, L.; Wang, H. Research on Flow-Induced Vibration and Energy Harvesting of Three Circular Cylinders with Roughness Strips in Tandem. *Energies* **2018**, *14*, 2977. [CrossRef]
39. Antonio, B.G.; David, V.L.; David, G.; Francisco, S. Enhance of Energy Harvesting from Transverse Galloping by Actively Rotating the Galloping Body. *Energies* **2020**, *13*, 91. [CrossRef]
40. Meynen, S.; Verma, H.; Hagedorn, P.; Schafer, M. On the Numerical Simulation of Vortex-Induced Vibrations of Oscillating Conductors. *J. Fluid Struct.* **2005**, *21*, 41–48. [CrossRef]
41. Clunia, F.; Gusellaa, V.; Bartoli, G. Wind Tunnel Scale Model Testing of Suspended Cables and Numerical Comparison. *J. Wind. Eng. Ind. Aerod.* **2008**, *96*, 1134–1140. [CrossRef]
42. Diana, G.; Manenti, A.; Melzi, S. Energy Method to Compute the Maximum Amplitudes of Oscillation of Bundle Conductors Due to Ice Galloping. *J. IEEE Trans. Power Deliv.* **2021**, *36*, 2804–2813. [CrossRef]
43. Nayfeh, A.H.; Arafat, H.N.; Chin, C.M.; Lacarbonara, W. Multimode interactions in suspended cables. *J. Vib. Control.* **2002**, *8*, 337–387. [CrossRef]
44. Yu, P.; Desai, Y.M.; Shah, A.H.; Popplewell, N. Three-Degree-of-Freedom Model for Galloping. Part I: Formulation. *J. Eng. Mech.* **1993**, *119*, 2404–2425. [CrossRef]
45. Takeuchi, M.; Maeda, J.; Ishida, N. Aerodynamic Damping Properties of Two Transmission Towers Estimated by Combining Several Identification Methods. *J. Wind. Eng. Ind. Aerod.* **2010**, *98*, 872–880. [CrossRef]
46. Tamura, Y.; Suganuma, S. Evaluation of Amplitude-Dependent Damping and Natural Frequency of Buildings During Strong Winds. *J. Wind. Eng. Ind. Aerod.* **1996**, *59*, 115–130. [CrossRef]